



Lawrence Berkeley Laboratory

UNIVERSITY OF CALIFORNIA

Physics, Computer Science & Mathematics Division

Submitted to the Journal of the Optical Society of America

PRINCIPLES OF TOMOGRAPHICAL IMAGING WITH LIMITED-ANGLE INPUT

K.C. Tam and V. Perez-Mendez

September 1980

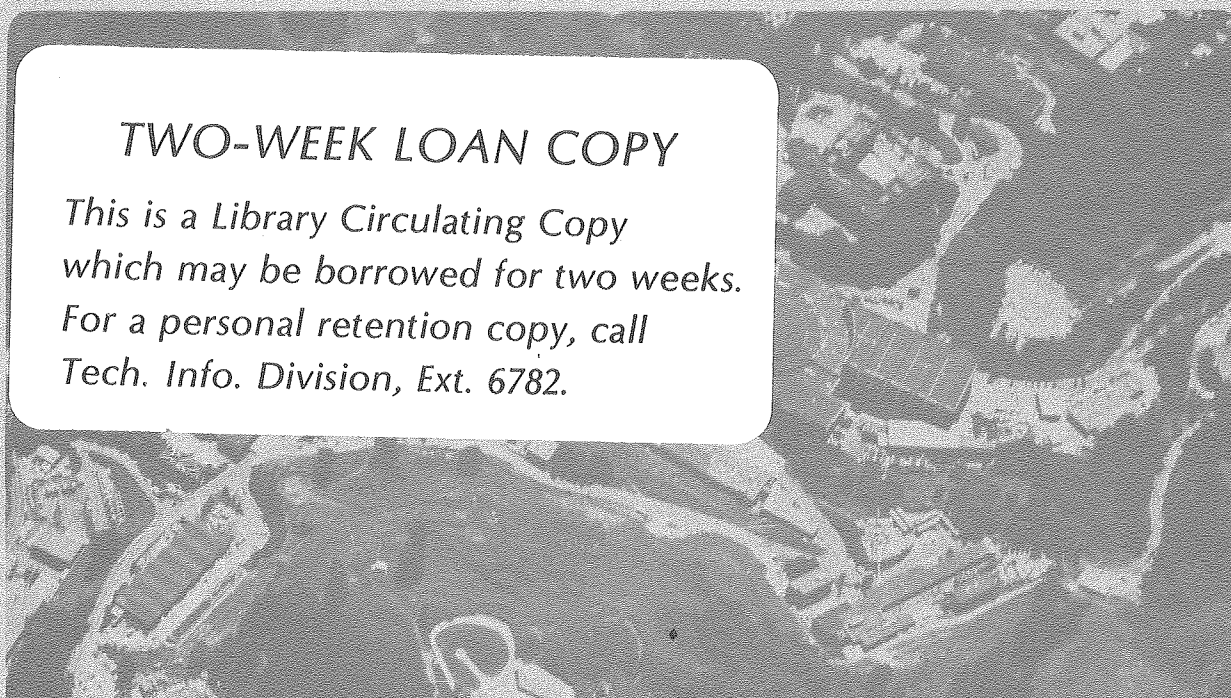
RECEIVED
LAWRENCE
BERKELEY LABORATORY

NOV 20 1980

LIBRARY AND
DOCUMENTS SECTION

TWO-WEEK LOAN COPY

*This is a Library Circulating Copy
which may be borrowed for two weeks.
For a personal retention copy, call
Tech. Info. Division, Ext. 6782.*



LBL-11589 c.2

DISCLAIMER

This document was prepared as an account of work sponsored by the United States Government. While this document is believed to contain correct information, neither the United States Government nor any agency thereof, nor the Regents of the University of California, nor any of their employees, makes any warranty, express or implied, or assumes any legal responsibility for the accuracy, completeness, or usefulness of any information, apparatus, product, or process disclosed, or represents that its use would not infringe privately owned rights. Reference herein to any specific commercial product, process, or service by its trade name, trademark, manufacturer, or otherwise, does not necessarily constitute or imply its endorsement, recommendation, or favoring by the United States Government or any agency thereof, or the Regents of the University of California. The views and opinions of authors expressed herein do not necessarily state or reflect those of the United States Government or any agency thereof or the Regents of the University of California.

PRINCIPLES OF TOMOGRAPHICAL IMAGING WITH LIMITED-ANGLE INPUT

K. C. Tam and V. Perez-Mendez

Lawrence Berkeley Laboratory, Berkeley, California 94720 and

Radiology Department, University of California,

San Francisco, California 94143

The theory of tomographical imaging with limited-angular input is discussed, from which two reconstruction algorithms are derived. The existence of missing information due to incomplete angular coverage is demonstrated, and an iteration algorithm to recover this information from a priori knowledge on the finite extent of the object developed. Smoothing algorithms to stabilize reconstructions in the presence of noise are given. The effects of digitization and finite truncation of the reconstruction region in numerical computation are also analysed. It is shown that the limited-angle problem is governed by a set of eigenvalues whose spectrum is determined by the imaging angle and the finite extent of the object. The distortion on a point source caused by the missing information is calculated; from the results some properties of the iteration scheme, such as spatial uniformity, are derived.

This manuscript was printed from originals provided by the author.

I. INTRODUCTION

In radiology and nuclear medicine imaging, information on the density distribution of an object is usually inferred from the radiation transmitted through or emitted from the object. Such methods of medical imaging, known respectively as transmission and emission tomography, usually involve collecting the radiation events while viewing the object from a continuous range of angles, or series of discrete angles, and then reconstructing the object distribution from the data. Object distributions can be two-dimensional, such as in ring positron cameras [1] and x-ray scanning (parallel beam or fan beam geometry) [2,3], as shown in Figure 1, or three-dimensional as in planar positron cameras [4] and pinhole imaging devices [5], as shown in Figure 2. Similar techniques have also been employed in other non-medical imaging situations, such as electron microscopy, radioastronomy, etc. In this paper we investigate the relationship between the angular range of the input data and the possibility of reconstructing the object distribution completely. We shall be dealing with objects of finite extent, digitized on a finite-spacing grid. This is a necessary requirement due to the finite resolution of all detectors and to the limitations of the computational techniques.

In Section II the basic imaging problem is formulated as a convolution equation, together with two algorithms to tackle it: one involving complete deconvolution and the other partial

deconvolution. The existence of a region of undetermined Fourier components in limited-angle imaging is shown in Section III. Section IV deals with the effects of digitization and finite truncation, whereas Section V treats the stability problem in the two reconstruction methods. In Section VI the possibility of recovering the undetermined Fourier components is discussed and two iteration schemes to achieve this purpose are proposed. In Section VII the effects of the undetermined Fourier components on a point source are evaluated; from these effects further properties of the iteration schemes are derived. In Section VIII the two reconstruction algorithms are compared, and some concluding remarks are given in Section IX.

II. BASIC EQUATION AND METHODS OF SOLVING

We shall take the line at the center of the measured data cone to be the z -axis. Due to the symmetry of the x and y axes in most cases, we shall write out only the x -axis explicitly and suppress the y coordinates in most of the mathematical treatment and figures in order to facilitate presentation.

In emission imaging, each point source in an object distribution generates a flux of gamma rays at each location in space. The flux pattern at \underline{r} due to a point source at \underline{r}' can be represented by constructing a scalar field $\phi_0(\underline{r}, \underline{r}')$ from the recorded events emitted by the point source in the limit where the number of such events becomes large. Hereafter we shall refer to ϕ_0 as

the point response function. Point response functions can be constructed in a variety of ways. The simplest way is to count the number of gamma rays that traverse a small test area element oriented at a particular angle at each location in space, as shown in Figure 3. This approach yields the conventional back projection tomograms. To generalize, one can weight each emission event as a function of the angle between the event and a fixed direction. Angular weighting can improve the signal-to-noise ratio in the data in those imaging devices where the error distribution in the data has an angular dependence. For example, noise in a planar positron camera due to Compton scattering concentrates in the small angle region [6], and therefore could be reduced by any angular weighting which emphasizes the large angle events.

The resultant effect at \underline{r} due to all the point sources in the object distribution $\rho(\underline{r}')$ is a scalar field $\phi(\underline{r})$ which is the linear superimposition of the flux generated by all the point sources within $\rho(\underline{r}')$, i.e.

$$\phi(\underline{r}) = \int \rho(\underline{r}') \phi_o(\underline{r}, \underline{r}') d^3r' \quad \text{-----} \quad (1)$$

In this equation it is assumed that the same angular weighting has been employed in constructing ϕ and ϕ_o .

In the case of transmission imaging, each volume element attenuates the intensity of the x-ray beams exponentially, and the total attenuation is the product of the individual attenuations.

Since taking the logarithmic function converts a product into a sum, Equation (1) also holds in the case of transmission imaging if the quantities ϕ and ϕ_0 are constructed from the logarithmic function of the attenuation in the appropriate directions. Equation (1) is therefore the basic equation relating the data to the object distribution in imaging.

As it stands, Equation (1) is difficult to solve in general. However, if the kernel is space invariant, i.e. $\phi_0(r, r') = \phi_0(r - r')$, then Equation (1) becomes

$$\phi(\underline{r}) = \int \rho(\underline{r}') \phi_0(\underline{r} - \underline{r}') d^3r' \quad \text{-----} \quad (2)$$

Solving for $\rho(\underline{r})$ is simplified considerably since various methods of solving integral equations with a kernel of such form have been developed [7]. In complete-angle imaging ϕ_0 is always space-invariant. In the limited-angle case, ϕ_0 can be made space-invariant by using only those events falling within a universal cone, which is the intersection of the detection cones subtended by all the point sources in the object. Further discussion on the construction of ϕ_0 and its space-invariance can be found in [8].

The solution of the two- or three-dimensional integral Equation (2) as a matrix equation on a digital computer requires a large amount of computation and core memory. A more practical approach is to Fourier transform the equation to frequency space.

As shown in [7], the transformed equation is diagonal, so the integral equation reduces to an algebraic equation,

$$\phi(\underline{k}) = \phi_o(\underline{k})R(\underline{k}) \quad \text{-----} \quad (3a)$$

where

$$\phi_o(\underline{k}) = \int \phi_o(\underline{r}) \exp(2\pi i \underline{k} \cdot \underline{r}) d^3r$$

$$\phi(\underline{k}) = \int \phi(\underline{r}) \exp(2\pi i \underline{k} \cdot \underline{r}) d^3r$$

$$R(\underline{k}) = \int \rho(\underline{r}) \exp(2\pi i \underline{k} \cdot \underline{r}) d^3r$$

The solution is given by

$$\rho(\underline{r}) = \int R(\underline{k}) \exp(-2\pi i \underline{k} \cdot \underline{r}) d^3k \quad \text{-----} \quad (3b)$$

where

$$R(\underline{k}) = \begin{cases} \frac{\phi(\underline{k})}{\phi_o(\underline{k})} & \text{if } \phi_o(\underline{k}) \neq 0 \\ \text{undetermined if } \phi_o(\underline{k}) = 0 \\ \text{(since here Equation (3a) becomes } 0 = 0) \end{cases} \quad \text{-----} \quad (3c)$$

If we Fourier transform Equation (2) only in the x dimension, we get the one-dimensional integral equation

$$\psi(k_x, z) = \int_{-\infty}^{\infty} \psi_o(k_x, z-z') p(k_x, z') dz' \quad \text{-----} \quad (4a)$$

where

$$\psi_o(k_x, z) = \int_{-\infty}^{\infty} \phi_o(x, z) \exp(2\pi i k_x x) dx$$

$$\begin{aligned}\psi(k_x, z) &= \int_{-\infty}^{\infty} \phi(x, z) \exp(2\pi i k_x x) dx \\ p(k_x, z) &= \int_{-\infty}^{\infty} \rho(x, z) \exp(2\pi i k_x x) dx\end{aligned}$$

and the solution is given by

$$\rho(x, z) = \int_{-\infty}^{\infty} p(k_x, z) \exp(-2\pi i k_x x) dk_x \quad (4b)$$

where

$$p(k_x, z) = \sum_i \frac{\int_{-\infty}^{\infty} g_i^*(k_x, z) \psi(k_x, z) dz}{\alpha_i} g_i(k_x, z) \quad (4c)$$

Here α_i , g_i are the eigenvalues and eigenfunctions of the integral operator (4a).

Equations (3) and (4) represent two methods of solving for $\rho(\underline{r})$. The former solves for the unknown $R(k_x, k_z)$ in frequency space and then inverse transforms in the k_x and k_z dimensions back to object space, whereas the latter tackles the problem in the k_x and z space followed by inverse transformation in the k_x dimension. Thereafter in the paper we shall refer to these methods as the deconvolution method [8,9], and the matrix method [10], respectively, since the one-dimensional integral equation (4a) becomes a matrix equation when solved on a digital computer.

III. THE OPTICAL TRANSFER FUNCTION AND THE UNDETERMINED FREQUENCY COMPONENTS

In order to reconstruct the object uniquely using the

deconvolution method from Equation (3c), all the frequency components of the optical transfer function $\phi_o(\underline{k})$ must be non-zero. For the matrix method, the corresponding requirement is that the integral operator in (4a) does not have zero eigenvalues [11]. Neither of these two conditions holds when (i) the ranges of integration involved cover all space, and (ii) the point response function does not have a complete angular coverage. To show this, we first calculate the optical transfer function $\phi_o(\underline{k})$. Due to a property of the data in transmission and emission imaging to be shown later (Equation (5)), we make the following coordinate transformation:

$$r(x,z) \rightarrow r(\theta,z)$$

$$\text{where } \theta = \tan^{-1}\left(\frac{x}{z}\right)$$

$$z = z$$

As mentioned in Section II, the general point response function at (x,z) is defined as the number of events, emitted from the point source, which pass through a line segment of unit length at (x,z) oriented at a certain angle, perpendicular to the z -axis for example, with each event weighted by a factor $F(\theta)$ depending on the angle θ the event makes with the z -axis. $F(\theta)$ is positive inside the cone and zero outside; the case of $F(\theta) = 1$ inside the cone corresponds to the conventional tomograms obtained from back-

projecting the events. For $z \neq 0$, consider a line segment dx pointing along the x -axis centered at (θ, z) relative to the point source (Fig. 4a)

$$\begin{aligned}\phi_o(\theta, z) &= F(\theta) \frac{\text{angle subtended by } dx \text{ at origin}}{\pi} \frac{1}{dx} \\ &= \frac{F(\theta)}{\pi} \frac{\cos^2 \theta}{|z|}\end{aligned}$$

Thus

$$\phi_o(\theta, z)|z| = \frac{F(\theta)\cos^2 \theta}{\pi} \quad (5)$$

Equation (5) shows that $\phi_o(\theta, z)|z|$ is a function of θ only. This expression is valid also at $z = 0$. The optical transfer function is

$$\Phi_o(k_x, k_z) = \int_{-\infty}^{\infty} dz \int_{-\infty}^{\infty} dx \phi_o(x, z) \exp(2\pi i(k_x x + k_z z)) \quad (6)$$

Performing this integral (Appendix A) we get

$$\Phi_o(k_x, k_z) = \begin{cases} \frac{\delta(z)}{\pi} \int_{\theta_o}^{\theta_o} F(\theta) d\theta & \text{if } k_x = 0 \\ \frac{1}{\pi|k_x|} F(\theta_i) \cos^2 \theta_i & \text{if } k_x \neq 0 \end{cases}$$

where $\tan \theta_i = \frac{-k_z}{k_x}$

Figure 4b shows schematically the shape of the two-dimensional optical transfer function. Three-dimensional point response functions and optical transfer functions are treated in Appendix B,

and the result (B.3) for the pyramidal $\phi_o(\underline{r})$ is illustrated in Figure 5. Figures 4b and 5b show that if ϕ_o does not have a complete angular coverage there are regions in frequency space where $\phi_o(\underline{k})$ is zero, and thus $R(\underline{k})$ cannot be recovered by the deconvolution method from Equation (3). The necessary and sufficient conditions for complete angular coverage for a three-dimensional point response function ϕ_o have been given in [12]. Hereafter we shall refer to the region where $\phi_o(\underline{k}) \neq 0$ as the "allowed cone" and that where $\phi_o(\underline{k}) = 0$ as the "missing cone", respectively.

The existence of the missing cone can also be shown in a simple way using the projection theorem [13], which states that the one-dimensional Fourier transform of the projection $P(r, \theta)$ of a two-dimensional function gives the components of the two-dimensional Fourier transform of the function on a line at angle $(\theta + \pi/2)$. Now it can be shown easily from Equation (5) that the total integrated intensity of $\phi_o(x, z)$ on any line which intercepts the detection cone completely is a constant independent of the position of the line. This means that the projection $P(r, \theta)$ of $\phi_o(x, z)$ is a constant function in r for $\theta (= \tan^{-1}(x/z))$ is the range $(\theta_o, \pi - \theta_o)$, and therefore its Fourier transform is a delta function at the origin.

In the case of the matrix method, we claim that the integral operator (4a) does have zero as its eigenvalue for every value of

k_x if ϕ_0 does not possess complete angular coverage. First we show that $\{\exp(-2\pi i k_z z)\}$ is the set of eigenfunctions of the integral operator. Setting $p(k_x, z) = \exp(-2\pi i k_z z)$, the integral becomes

$$\begin{aligned} & \int_{-\infty}^{\infty} \psi_0(k_x, z-z') \exp(-2\pi i k_z z') dz' \\ &= \exp(-2\pi i k_z z) \phi_0(k_x, k_z) \end{aligned}$$

Thus $\{\exp(-2\pi i k_z z)\}$ is the set of eigenfunctions of the integral operator with eigenvalues $\phi_0(k_x, k_z)$. However, we have already shown that ϕ_0 has zero components if it does not possess complete angular coverage. Since the eigenfunctions form a complete set, the general solution of the integral equation (4a) is

$$p(k_x, z) = \int_{-\infty}^{\infty} C(k_x, k_z) \exp(-2\pi i k_z z) dk_z$$

where the coefficients $C(k_x, k_z)$ are given by

$$C(k_x, k_z) = \begin{cases} \frac{\int_{-\infty}^{\infty} \psi(k_x, z) \exp(2\pi i k_z z) dz}{\phi_0(k_x, k_z)} = \frac{\phi(k_x, k_z)}{\phi_0(k_x, k_z)}, & \text{if } \phi_0(k_x, k_z) \neq 0 \\ \text{undetermined, if } \phi_0(k_x, k_z) = 0 \end{cases}$$

The solution $\rho(x, z)$ in object space is obtained by inverse transforming $p(k_x, z)$ in the k_x dimension, and it can be seen that the result is identical to that obtained by the deconvolution method, as expected.

It follows that $\rho(x,z)$ cannot be determined uniquely using either the deconvolution method or the matrix method represented by Equations (3) and (4), respectively, if the point response function does not have a complete angular coverage and no further information is available.

IV. EFFECTS OF DIGITIZATION AND FINITE TRUNCATION

In practical imaging situations, due to limitation in detector resolution and digital computation, object distributions are always analysed on a finite grid of points with finite spacings Δx , Δz . Besides limiting the frequency range to

$$|k_x| \leq \frac{1}{2\Delta x}, \quad |k_z| \leq \frac{1}{2\Delta z},$$

digitization also changes the shape of the point response function. As mentioned in Section III, the vanishing of $\phi_0(k_x, k_z)$ in the missing cone is due to the property of $\phi_0(x, z)$ as expressed in Equation (5). However, if $\phi_0(x, z)$ is digitized, Equation (5) is no longer applicable, and hence part or all of the zero values in the missing cone become non-zero, as shown in the detailed analysis in Appendix C. The result of this analysis shows that the undetermined components of $R(\underline{k})$ are eliminated if sampled in the x and z dimensions. For the matrix method, the eigenfunctions with zero as eigenvalue are also eliminated in a corresponding manner. In other words, digitization makes it possible to

reconstruct object distributions completely.

Another limitation imposed by digital computation is that reconstructions can only be performed in a finite region of space of finite dimension $L_x \times L_z$. As a consequence, the point response function becomes space variant and so the integral in Equation (2) is no longer a convolution, thus introducing some error into the solutions obtained by the deconvolution or matrix methods. However, if the half-angle of the detection cone and the dimensions L_x, L_z are such that the detection cones generated at every point in the object do not intersect the vertical edges of the reconstruction region, as illustrated in Figure (6), the space invariance of ϕ_0 in the x dimension is preserved. That means the convolution relation in the x dimension is still valid, and so the matrix method solution remains exact.

Besides the discreteness in resolution, the data in some imaging devices are taken in a number of discrete angles. It is well known that an object cannot be reconstructed from a finite number of projections. However, if a priori information is evoked, only a negligible amount of information is lost if the angular sampling is dense enough. This point will be elaborated in more detail in Section VI.

V. INSTABILITIES

As shown in Section II, each Fourier component $\phi(k_x, k_z)$ of

the data $\phi(x,z)$ is multiplied by the factor $1/\phi_0(k_x, k_z)$ in deconvolution; in the matrix method, each eigenfunction component is also amplified by the factor $1/(\text{eigenvalue})$. As a result, instabilities arise where the $\phi_0(k_x, k_z)$'s or the eigenvalues are small.

One way to minimize these instabilities is to impose on the solution the smoothness condition adopted by Phillips [14]:

$$\int [\nabla^2 \rho(\underline{r})]^2 d^3r = \text{minimum} \quad \text{-----} \quad (7)$$

For deconvolution, the net effect of this smoothing procedure is to introduce an additional term in the denominator of Equation (3c) as shown in [8]:

$$R(\underline{k}) = \frac{\phi(\underline{k})}{\phi_0(\underline{k}) + \gamma \frac{(2\pi)^4 k^4}{\phi_0(\underline{k})}} \quad \text{-----} \quad (8)$$

where $\gamma(>0)$ is an adjustable parameter which depends on the noise level. This additional term is negligible at low frequencies compared to $\phi_0(\underline{k})$, but increases rapidly in magnitude with frequency as both k^4 increases and $|\phi_0(\underline{k})|$ decreases. Thus the information at low frequencies is suppressed.

The additional term also plays a significant role in the missing-cone region. As shown in the previous section, digitization makes the Fourier components $\phi_0(k_x, k_z)$ in the missing-cone region non-zero. These components, however, are very small in magnitude, and thus error amplification in the deconvolution

Equation (3c) is especially serious in this region. Even in the ideal case that the data $\phi(x,z)$ contains no error, the error produced in $\phi(k_x, k_z)$ due to the space variance of the point response function arising from space truncation alone will render the information in the missing-cone region unreliable. The effect of the additional term in Equation (8) is to set $R(k)$ close to zero in the missing-cone region. This means that for the deconvolution method, the information in the missing-cone region is always unavailable. The lack of information on the missing-cone components introduces non-uniqueness into the solution. Setting these missing-cone components to zero gives a minimum norm solution, a consequence of Parseval's theorem, but it is clearly not the correct solution.

The effect of imposing the smoothness condition (7) on the matrix method solution is very similar to that on the deconvolution. For every value of k_x , instead of solving the ill-conditioned matrix equation

$$Y = AX$$

which is the digital version of Equation (4a), another matrix equation with a modified kernel [15] is solved:

$$Y = \{A + \gamma G[(2\pi k_x)^2 I + \frac{C}{\Delta z^2}]^2\}X \quad \text{-----} \quad (9)$$

Here Δz is the grid spacing in the z direction, I is the identity

matrix, G is the left generalized inverse of the matrix A , and the matrix C is given by

$$c_{ij} = \begin{cases} -2 & i = j \\ 1 & i = j+1 \\ 0 & \text{otherwise} \end{cases}$$

VI. EFFECTS OF THE KNOWLEDGE ON THE FINITE EXTENT OF THE OBJECT

($\rho(x,z) \neq 0$ for $x_1 \leq x \leq x_2$, $z_1 \leq z \leq z_2$)

As stated in Section IV, taking data in a finite number of discrete angles gives rise to non-unique solutions. However, by making use of the fact that the object is finite in extent, this non-uniqueness can be removed. Klug and Crowther [16] have shown that for a 2-dimensional object of diameter D which is digitized in pixels of dimension d , m projections at equally spaced angles from 0 to π contain almost all the information required to reconstruct the object uniquely, where m is given by

$$m \approx \frac{\pi D}{2d}$$

The undetermined Fourier components in the missing cone can be recovered by making use of the knowledge on the finite extent of the object, a consequence of two theorems: (1) the Fourier transform of a finite object is an entire function, and (2) an entire function can be continued throughout the whole complex plane from a knowledge of the function on any finite continuous

line segment [17]. As a result, $R(k_x, k_z)$ can be continued throughout the k -space from a knowledge of the function within the cone. The procedure cannot be used when $\theta_0 = 0$, since then the only region in which $R(\underline{k})$ is known is the line $k_z = 0$ which therefore contains no interior points.

The above analysis shows that all the information on any density distribution of finite extent is contained in its Fourier components within any open cone in frequency space with its apex at the origin. This conclusion is in agreement with the fact that such a distribution is uniquely determined by any infinite set of projections [18,19].

In the case of the matrix method, it is convenient to consider first the finiteness of the object in the z direction, which is built into the method, followed by that in the x direction. As shown in Appendix D, the integral operator (4a) in the matrix method becomes positive definite when the range of integration in z is finite, and by [11], the eigenfunctions associated with it form a complete set in the class of functions square integrable in (z_1, z_2) , and thus unique solutions exist for the integral operator. This argument breaks down if $k_x \tan \theta_0 = 0$. Therefore, there is no unique solution for $p(k_x, z)$ if $k_x = 0$ or $\theta_0 = 0$. For the general case $\theta_0 > 0$, the only missing information is $p(0, z)$ for each $z_1 \leq z \leq z_2$ (see Fig. (7)). These undetermined components at $k_x = 0$ on each z -plane can be filled in from values at $k_x \neq 0$

on the same z -plane by virtue of the fact that $p(k_x, z)$ is entire in k_x for all $z_1 \leq z \leq z_2$ (since $p(x, z)$ is non-zero only for $x_1 \leq x \leq x_2$). If $\theta_0 = 0$, the components at $k_x \neq 0$ are not known themselves, not to mention the continuation to $k_x = 0$.

To implement the continuation process, the most direct approach would be to calculate the successive derivatives of $R(\underline{k})$ at some point k_0 in the allowed cone to form a Taylor series expansion of $R(\underline{k})$ which converges everywhere. In practice such a series has to be truncated, so the error for the values of the series calculated at a region far away from k_0 would be large. In addition, it is difficult to determine accurately the derivatives of a function numerically.

Another method for the continuation of an analytic function is by means of a prolate spheroidal function expansion [20,21]. The function $R(\underline{k})$ to be continued is expanded in a series of prolate spheroidal function $\psi_i(\underline{k})$

$$R(\underline{k}) = \sum_i a_i \psi_i(\underline{k})$$

the coefficients a_i being determined from the known values of $R(\underline{k})$ in the allowed cone.

A Fourier series expansion can also be used in extending the function to fill in the missing cone. This method was employed by Harris [17] to continue a one-dimensional spectrum, and by Inouye [22] to reconstruct a two-dimensional image.

A practical way to recover the missing-cone components is the iteration scheme given below [23]. The object is Fourier transformed back and forth between the object space and the Fourier space, being corrected in each step by the known Fourier components in the allowed cone and the known finite extent of the object. An alternate approach is to use the Radon transform to manipulate the object back and forth between the projection space and the object space, the constraints being the known projections in the limited angular range and the known finite extent of the object [24]. These two iteration methods are shown schematically in Figures 8 and 9.

The convergence property of the Fourier transform iteration scheme can be understood in terms of two operators A and B operating on any Fourier transformable function f defined in frequency space. A and B are defined as follows:

$$Af = \chi_A f$$

$$Bf = F^{-1} \chi_B Ff$$

where F and F^{-1} represent the Fourier transformation and its inverse. χ_A, χ_B are, respectively, the characteristic functions of the allowed cone, R_a , in Fourier space and of the object region, R_b , in object space (Fig. 10), and are defined as:

$$x_A(\underline{k}) = \begin{cases} 1 & \underline{k} \in R_a \\ 0 & \underline{k} \notin R_a \end{cases}$$

$$x_B(\underline{x}) = \begin{cases} 1 & \underline{x} \in R_b \\ 0 & \underline{x} \notin R_b \end{cases}$$

With these operators, it can be shown that the truncation error $E_t^{(n)}(\underline{k})$ in terminating the iteration after n steps is given by:

$$E_t^{(n)}(\underline{k}) = -\sum_i a_i (1 - \lambda_i)^n \psi_i(\underline{k}) \quad 0 < \lambda_i < 1 \quad \text{--- (10)}$$

where λ_i, ψ_i are the eigenvalues and eigenfunctions of the operator BA , and a_i are the expansion coefficients of $R(\underline{k})$ in terms of ψ_i 's. The derivation of Equation (10) was given in [25]. Equation (10) shows that the major source of error comes from those eigenfunctions associated with the small eigenvalues for which $(1 - \lambda_i)^n$ goes to zero only very slowly with n .

The eigenvalues of BA for a square-shaped object boundary have been calculated for various half-angles of the allowed cone. The results are shown in Figure 11. It can be seen that every spectrum can be roughly divided into two regions, one in which the eigenvalues are close to unity and the other with eigenvalues close to zero. As iterations proceed, those components of the truncation error $E_t^{(n)}(\underline{k})$ corresponding to the larger eigenvalues (~ 1) will go to zero very rapidly, while those corresponding to the smaller eigenvalues (~ 0) will approach zero only very slowly.

As a result, $E_t^{(n)}(k)$ is expected to level off after an initial relatively rapid decrease with iterations. To show this effect the Fourier transform iteration algorithm was applied to restore the missing-cone components of a 2-D phantom. The reconstruction area is a 128 x 32 lattice, with equal lattice spacings in the $x(i)$ and $z(k)$ directions. The phantom has a square boundary with perpendicular diagonals which are both 11 lattice spacings long in the x and z directions, respectively. The allowed cone has a half-angle of $\tan^{-1}(0.5)$ and is centered around the k_x -axis. The Fourier components of the phantom outside the allowed cone were first set to zero, and then the iteration scheme was employed to recover them. Figure 12 shows the root mean square error σ of the reconstruction as a function of iterations; here σ is defined as

$$\sigma = \sqrt{\frac{\sum_{i,k} (\text{reconstruction } (i,k) - \text{phantom } (i,k))^2}{\text{number of pixels}}}$$

The results demonstrate the levelling off of $E_t^{(n)}$ after an initial rapid decrease with iterations.

Figure 11 also shows that as the opening angle of the allowed cone decreases the region of small eigenvalues grows, hence the truncation error is expected to increase with decrease in the allowed-cone angle. This behavior is clearly shown in Figure 13, where the root mean square error σ of the reconstructed image

after 20 iterations is plotted as a function of the half-angle of the allowed cone for the 2-D phantom mentioned above.

VII. EFFECTS OF THE MISSING CONE ON A POINT SOURCE

The effect of setting the missing-cone components to zero on a point source has been mentioned in previous papers [25,26]. In Reference 24 this effect was analysed in more detail in two dimensions. Besides casting light on the nature of the distortion caused by the missing cone, results of the analysis are also useful in understanding the spatial uniformity of reconstructed objects.

Assume a point source is located at the origin $x = z = 0$. With the Fourier components in the missing cone set to zero, the distorted point source $\rho'(x,z)$ is given by [24]

$$\rho'(x,z) = \frac{1}{\pi^2(\tan\theta_0 z^2 - \frac{x^2}{\tan\theta_0})} \quad \text{for } (x,z) \neq (0,0) \quad (11)$$

Equation (11) shows that the distortion is positive in the cones $|x| < \tan\theta_0 |z|$, and negative in the cones $|x| > \tan\theta_0 |z|$. In an extended object, most of the negative distortion will be swamped by the positive densities at other positions in the object. Therefore, the use of a positivity constraint in iterations, i.e. resetting all negative densities to zero, improves convergence significantly for point sources but not for extended objects, as reported in [25].

The positive distortion in the region $|x| < \tan\theta_0|z|$ rises to high positive values in the immediate vicinity of the lines $x = \pm \tan\theta_0 z$; the negative distortion in the region $|x| > \tan\theta_0|z|$ also becomes large near the lines. These high positive and negative values give rise to what appear to be four ridges originating from the point source and decaying with distance: two positive ones and two negative ones bordering the lines $x = \pm \tan\theta_0 z$. These distortions are singular and discontinuous in crossing the boundary between the positive and negative regions. These singularities and discontinuities are smeared out in digital Fourier transformation and averaged out to small finite values.

The distortion of a point source caused by the missing-cone components is shown graphically in Figure 14. The half-angle of the allowed cone is $\tan^{-1}(0.5)$. Figure 14A shows the positive density distribution of the distorted point source, and Figure 14B shows the negative density distribution. The presence of the two positive and the two negative ridges originating from the point source, and the elongation of the point source along the z-axis are evident. The other smaller ridges not originating from the point source are due to the sharp cut-off of the Fourier area.

The positive distortion in the cones $|x| < \tan\theta_0|z|$ makes the point source appear elongated in the z direction. When the half-angle θ_0 of the allowed cone is small, elongation along the z-axis ($x = 0$) is especially serious, as implied in Equation (11),

and contains most of the distortion energy of the distorted point source. If part or all of this elongation is repeatedly reset to zero during iterations, convergence will be very rapid. Thus, at small allowed-cone angles, convergence of the iteration scheme is primarily determined by whether or not the point source is located in a position where part or all of its elongation extends outside the object boundary and thus is repeatedly reset to zero during iterations.

The above discussion can be made clear by considering the situation in Figure 15. The 32×32 array is the reconstruction area, while the 11×11 square area in the middle of the array represents the finite extent of an object: anything outside the square is reset to zero during iterations. As far as the convergence of the iterations is concerned, the pixel A(16,17) in Figure 15 is the worst location within the square boundary because a point source at this position has the largest fraction of its ridges inside the square boundary, whereas pixel B(16,22), similar to the other pixels on the top and bottom edges, represents the best location since half of each ridge is outside the boundary for a point source located at B. For pixel C(21,17) and the other pixels on the left and right edges, half of each ridge is also outside the boundary, but all of the elongated portion is still inside; thus a point source at C is not expected to do much better than at A. The above statements have been verified experimentally

[24]. The results show that at small angles the elongated portion along the z-axis is the main factor determining the convergence of the iterations, and therefore the densities in all the pixels are reconstructed to the same fidelity, except for the ones on the very top and bottom edges.

As the angle of the allowed cone increases, the distortion amplitude becomes more spread out in the ridges and on the x-axis. As a result, more pixels near the boundary will be reconstructed better than the interior pixels. However, since the convergence of the iteration scheme improves rapidly with the increase in the allowed-cone angle, the reconstruction error would be small everywhere within the object boundary and thus could not cause any serious problem in spatial uniformity.

VIII. COMPARISON BETWEEN DECONVOLUTION + ITERATIONS AND MATRIX INVERSION

In principle, both the combined scheme of deconvolution + Fourier iterations and the matrix inversion method are capable of performing limited-angle reconstructions. In practical applications, however, the two algorithms show rather different characteristics. In the case of no noise or very low noise levels in the data, the matrix method has advantages over the deconvolution + iterations algorithm. The reasons are two-fold. First, the information on the finite extent of the object is built into the matrix method,

so no iterations are necessary. Second, in digital computations digitization removes the non-uniqueness due to limited-angle information, thus reconstruction is no longer a missing-cone problem and complete reconstruction is possible in one step with either the deconvolution or the matrix method, as discussed in Section IV. On the other hand, the finite truncation of the reconstruction area makes the point response function space-variant in the z dimension. This introduces an error into the deconvolution algorithm but not into the matrix inversion, thereby rendering the missing-cone components in the deconvolution algorithm unusable (see Sec. V).

The matrix method is very ill-conditioned, i.e. unstable with respect to noise propagation; on the other hand, the deconvolution + iterations approach is quite stable [25]. Therefore, when applied to practical data that contain significant amounts of noise, the deconvolution + iterations scheme gives better reconstructions.

The instabilities of the matrix method are especially serious at small values of $|k_x|$ [25]. One way to stabilize the matrix method is to discard the small $|k_x|$ components of the computation that contain most of the error, and, by making use of the finite extent of the object in the x dimension, fill in those components using the ones with higher $|k_x|$ values through the iteration scheme shown in Figure 16 [25]. In this iteration scheme there is an

arbitrariness in the choice of the value of k_0 such that a component at k_x is discarded if $|k_x| < k_0$. After the reconstructions from the matrix inversion are improved by this iteration procedure with an optimum choice of k_0 , our experience has shown that their quality is about the same as that from the combined deconvolution + Fourier iterations scheme.

IX. CONCLUDING REMARKS

Because of its stability, deconvolution followed by Fourier transform iterations is a practical way for limited-angle reconstruction in general imaging situations where noise is not negligible. The ultimate accuracy that can be attained is limited by the small eigenvalues of the BA operator. Since the eigenvalue spectrum is determined by the size of the angle of the allowed cone and the finite extent of the object, the fidelity of reconstructions can only be improved if we have more a priori knowledge on the object other than its finite extent and location. For example, if it is known that an object has circular symmetry, one projection will suffice to reconstruct it completely. However, besides the constraint of positivity which has been shown to be of little help in reconstructing extended objects (see Sec. VII), no other constraints of exact nature are available for general objects.

Entropy maximization, a constraint of probabilistic nature,

has been extensively used in image reconstruction [27,28]. We have investigated the possibility of using entropy maximization for limited-angle object reconstruction. Our work [29] shows that the entropy difference between the object reconstructed using only the allowed cone information as the initial step and the final object decreases rapidly at first as we perform the reconstruction iterations, and thereafter very slowly. From this and more general arguments given in [29] we conclude that the entropy maximization will not produce better reconstructions than the methods discussed here. Furthermore, the amount of computer time required to perform the entropy maximization is considerably higher.

ACKNOWLEDGEMENTS

We would like to thank Drs. B. Macdonald and A. Grunbaum for stimulating and helpful discussions.

This work was supported by the Physics, Computer Science and Mathematics Division of Lawrence Berkeley Laboratory, United States Department of Energy under contract No. W-7405-ENG-48.

APPENDIX A

EVALUATION OF THE TWO-DIMENSIONAL OPTICAL TRANSFER FUNCTION

$$\begin{aligned}
 \phi_o(k_x, k_z) &= \int_{-\infty}^{\infty} dz \int_{-\infty}^{\infty} dx \phi_o(x, z) \exp(2\pi i(k_x x + k_z z)) \\
 &= \int_{-\infty}^{\infty} dz \int_{-\pi}^{\pi} d\theta \phi_o(\theta, z) \exp(2\pi i z(k_x \tan \theta + k_z)) |z| \sec^2 \theta \\
 &= \int_{-\theta_0}^{\theta_0} d\theta \frac{F(\theta)}{\pi} \int_{-\infty}^{\infty} dz \exp(2\pi i z(k_x \tan \theta + k_z))
 \end{aligned}$$

Now

$$\int_{-\infty}^{\infty} \exp(2\pi i z(k_x \tan \theta + k_z)) dz = \delta(k_x \tan \theta + k_z) \quad \text{———— (A.1)}$$

therefore

$$\begin{aligned}
 \phi_o(k_x, k_z) &= \int_{-\theta_0}^{\theta_0} \frac{F(\theta)}{\pi} \delta(k_x \tan \theta + k_z) d\theta \\
 &= \begin{cases} \frac{\delta(k_z)}{\pi} \int_{-\theta_0}^{\theta_0} F(\theta) d\theta & \text{if } k_x = 0 \\ \frac{F(\theta_i) \cos^2 \theta_i}{\pi |k_x|} & \text{if } k_x \neq 0 \end{cases} \quad \text{———— (A.2)}
 \end{aligned}$$

$$\text{where } \tan \theta_i = -\frac{k_z}{k_x}$$

APPENDIX B

EVALUATION OF THE THREE-DIMENSIONAL OPTICAL TRANSFER FUNCTION

In three dimensions, Equation (5) takes the form

$$\phi_o(\underline{s}, z) |z|^2 = H(\underline{s}/z) \quad \text{-----} \quad (\text{B.1})$$

where $\underline{s} = (x, y)$, and the angular function H is positive inside the data cone and zero outside. Defining $\underline{t} = \underline{s}/z$, $\underline{w} = (k_x, k_y)$, and performing the Fourier transformation, we get

$$\begin{aligned} \phi_o(\underline{w}, k_z) &= \int dz \iint d^2s \phi_o(\underline{s}, z) \exp(2\pi i(\underline{w} \cdot \underline{s} + k_z z)) \\ &= \iint H(\underline{t}) \delta(\underline{w} \cdot \underline{t} + k_z) d^2t \end{aligned}$$

The vector $\underline{t} = (t_1, t_2)$ can be chosen so that t_1 lies along \underline{w} , giving $\underline{w} \cdot \underline{t} + k_z = |\underline{w}| t_1 + k_z$. Then we get

$$\phi_o(\underline{w}, k_z) = \begin{cases} \delta(k_z) \iint H(\underline{t}) d^2t & \text{if } \underline{w} = 0 \\ \int H(-k_z/|\underline{w}|, t_2) dt_2 & \text{if } \underline{w} \neq 0 \end{cases} \quad \text{-----} \quad (\text{B.2})$$

In the particular case where ϕ_o is in the form of a square pyramid, i.e.,

$$\phi_o(x, y, z) > 0 \quad \text{whenever } 0 \leq |x| \leq |z \tan \theta_o|$$

$$\text{and } 0 \leq |y| \leq |z \tan \theta_o|$$

application of (B.2) shows that

$$\begin{aligned}
 \Phi_0(k_x, k_y, k_z) &> 0 \text{ if } (|k_x| + |k_y|) > |k_z|/\tan\theta_0 \\
 &\quad \text{when } |k_x|, |k_y| > 0 \\
 \text{or } (|k_x| + |k_y|) &\geq |k_z|/\tan\theta_0 \\
 &\quad \text{when } |k_x| = 0 \text{ or } |k_y| = 0 \\
 &= 0 \text{ otherwise}
 \end{aligned}
 \tag{B.3}$$

APPENDIX C

EFFECTS OF SAMPLING $\phi_o(x,z)$ IN THE x AND z DIMENSIONS

Let the object distribution $\rho(\underline{r})$ be sampled in the z dimension by the sampling function:

$$s_{\Delta z}(z) = \sum_{n=-\infty}^{\infty} \delta(z - n\Delta z)$$

The point response function $\phi_o(x,z)$ can thus be sampled in the same way. By the convolution theorem, the optical transfer function $\phi_o^{(z)}(k_x, k_z)$ of the sampled $\phi_o(x,z)$ is given by

$$\phi_o^{(z)}(k_x, k_z) = \phi_o(k_x, k_z) * S_{\Delta k_z}(k_z) \quad \text{————— (C.1)}$$

where $\phi_o(k_x, k_z)$ is the original optional transfer function, $S_{\Delta k_z}(k_z)$ is the Fourier transform of $s_{\Delta z}(z)$, and $*$ denotes convolution. Now Reference [30] shows that $S_{\Delta k_z}(k_z)$ is also a sampling function in the k_z dimension given by

$$S_{\Delta k_z}(k_z) = \Delta k_z \sum_{n=-\infty}^{\infty} \delta(k_z - n\Delta k_z), \quad \Delta k_z = \frac{1}{\Delta z} \quad \text{————— (C.2)}$$

From Equations (C.1) and (C.2) we see that $\phi_o^{(z)}(k_x, k_z)$ is the superimposition of repetitions of the original optical transfer function in the k_z dimension at intervals of Δk_z . Thus $\phi_o^{(z)}(k_x, k_z)$ is non-zero in the region $2|k_x|\tan\theta_o \geq \Delta k_z$; as for the region $2|k_x|\tan\theta_o < \Delta k_z$, the number of zero Fourier components is reduced by a factor of 2.

If sampling of $\phi_0(x,z)$ is done in the x dimension instead, similar considerations show that the corresponding optical transfer function $\phi_0^{(x)}(k_x, k_z)$ will be non-zero everywhere.

APPENDIX D

PROOF FOR THE POSITIVE DEFINITENESS OF THE MATRIX INTEGRAL OPERATOR FOR OBJECTS FINITE IN z EXTENT

Recall that the kernel of the integral operator is in the form:

$$\mathcal{Y}_0(k_X, z-z') = \int_{-\theta_0}^{\theta_0} \frac{F(\theta)}{\pi} \exp(2\pi i k_X \tan \theta (z-z')) d\theta$$

For any function $f(z)$ piece-wise continuous and spatially bounded in $z_1 \leq z \leq z_2$,

$$\begin{aligned} & \int_{z_1}^{z_2} dz' \int_{z_1}^{z_2} dz \mathcal{Y}_0(k_X, z-z') f(z) f^*(z') \\ &= \int_{z_1}^{z_2} dz' \int_{z_1}^{z_2} dz \int_{-\theta_0}^{\theta_0} d\theta \frac{F(\theta)}{\pi} \exp(2\pi i k_X \tan \theta (z-z')) f(z) f^*(z') \\ &= \frac{1}{\pi} \int_{-\theta_0}^{\theta_0} F(\theta) \left| \int_{z_1}^{z_2} \exp((2\pi i k_X \tan \theta) z) f(z) dz \right|^2 d\theta \quad \text{————— (D.1)} \end{aligned}$$

Since $F(\theta) > 0$ for all $-\theta_0 \leq \theta \leq \theta_0$, the vanishing of Expression (D.1) would require that

$$\begin{aligned} I(k_X \tan \theta) &= \int_{z_1}^{z_2} \exp((2\pi i k_X \tan \theta) z) f(z) dz = 0 \\ &\text{for all } -|k_X \tan \theta_0| \leq k_X \tan \theta \leq |k_X \tan \theta_0| \end{aligned}$$

Now the integral $I(k_X \tan \theta)$ is an entire function [31]. If it is zero within the interval $[-k_X \tan \theta_0, k_X \tan \theta_0]$, it must be zero everywhere. Thus $f(z)$ must be zero everywhere. This argument proves that the integral operator

$$g(z) = \int_{z_1}^{z_2} \varphi_0(k_x, z-z') f(z') dz'$$

is positive definite.

REFERENCES

1. Robertson, J. S., Marr, R. B., Rosenblum, M., Radeka, V., and Yamamoto, Y. L., 1973, "32-Crystal Positron Transverse Section Detector," in: Tomographic Imaging in Nuclear Medicine, Ed. G. S. Freedman (New York: Society of Nuclear Medicine) pp. 142-153.
2. Hounsfield, G. N., "Computerized Transverse Axial Scanning (Tomography): Part I. Description of System," Br. J. Radiol, 46 (1973) 1016-1022.
3. McCullough, E. C., Payne, J. T., Baker, H. L., Hattery, R. R., Sheedy, R. F., Stephens, D. H., and Gedgaudus, E., "Performance Evaluation and Quality Assurance of Computer Tomography Scanners, with Illustrations from the EMI, ACTA and Delta Scanners," Radiology, 120 (1976) 173-188.
4. Lim, C. B., Chu, D., Kaufman, L., Perez-Mendez, V., and Sperinde, J., "Characteristics of Multiwire Proportional Chambers for Positron Imaging," IEEE Trans. Nucl. Sci., NS-21 (1974) 85-88.
5. Grant, D. G., "Tomosynthesis: a Three-dimensional Radiographic Imaging Technique," IEEE Trans. Bio-Med. Eng., BME-19 (1972) 20-28.
6. Tam, K. C., 1979, Limited-angle Imaging in Positron Cameras: Theory and Practice (Ph.D. Thesis), Section 3.1.2. University of California, Berkeley, California.

7. Morse, P. M., and Feshbach, H., 1953, Methods of Theoretical Physics (New York: McGraw-Hill) Part I; Chapter 8.
8. Chu, G., and Tam, K. C., "Three-dimensional Imaging in the Positron Camera using Fourier Techniques," Phys. Med. Biol., 22 (1977) 245-265.
9. Tam, K. C., Chu, G., Perez-Mendez, V., and Lim, B. C., "Three-dimensional Reconstructions in Planar Positron Cameras using Fourier Deconvolution of Generalized Tomograms," IEEE Trans. Nucl. Sci., NS-25 (1978) 152-159.
10. Chang, L. T., Macdonald, B., and Perez-Mendez, V., "Three-dimensional Image Reconstruction using Pinhole Arrays," IEEE Trans. Nucl. Sci., NS-23 (1976) 568.
11. Riesz, F., and Sz.-Nagy, B., 1955, Functional Analysis (New York: Frederick Ungar), Chapter 6.
12. Vainshtein, B. K., and Orlov, S. S., 1974, "General Theory of Direct 3-D Reconstruction," in: Techniques of Three-Dimensional Reconstruction: Proc. Int. Workshop, Brookhaven National Laboratory, Upton, New York, July 16-19, 1974 (Brookhaven National Laboratory, Upton, NY, USA).
13. Crowther, R. A., DeRosier, D. J., and Klug, A., "The Reconstruction of a Three-dimensional Structure from Projections and its Application to Electron Microscopy," Proc. Roy. Soc. Lond. A, 317 (1970) 319-340.

14. Phillips, D. L., "A Technique for the Numerical Solution of Certain Integral Equations of the First Kind," J. Ass. Comput. Mach., 9 (1962) 84-97.
15. Macdonald, B., private communication.
16. Klug, A., and Crowther, R. A., "Three-dimensional Image Reconstruction from the Viewpoint of Information Theory," Nature, 238 (1972) 435-440.
17. Harris J. L., "Diffraction and Resolving Power," J. Opt. Soc. Am., 54 (1964) 931-936.
18. Solmon, D. C., "The X-ray Transform," J. Math. Anal. Appl., 56 (1976) 61-83.
19. Smith K. T., Solmon. D. C., and Wagner, S. L., "Practical and Mathematical Aspects of the Problem of Reconstructing Objects from Radiographs," Bull. Amer. Math. Soc., 83 (1977) 1227-1270.
20. Slepian, D., and Pollak, H. O., "Prolate Spheroidal Wave Functions, Fourier Analysis and Uncertainty - I," Bell Syst. Tech. J., 40 (1961) 43.
21. Barnes, C. W., "Object Restoration in a Diffraction-Limited Imaging System," J. Opt. Soc. Am., 56 (1966) 575-578.
22. Inouye, T., "Image Reconstruction with Limited Angle Projection Data," IEEE Trans. Nucl. Sci., NS-26 (1979) 2666-2669.
23. Tam, K. C., Macdonald, B., and Perez-Mendez, V., "3-D Object Reconstruction in Emission and Transmission Tomography with Limited Angular Input," IEEE Trans. Nucl. Sci., NS-26 (1979) 2797-2805.

24. Tam, K. C., and Perez-Mendez, V., "Limited-Angle 3-D Reconstructions using Fourier Transform Iterations and Radon Transform Iterations," presented at the 1980 International Optical Computing Conference, Washington, D.C., April 7-11, 1980; also to be published in Optical Engineering.
25. Tam, K. C., Perez-Mendez, V., and Macdonald, B., "Limited Angle 3-D Reconstructions from Continuous and Pinhole Projections," IEEE Trans. Nucl. Sci., NS-27 (1980) 445-458.
26. Chiu, M. Y., Barrett, H. H., Simpson, R. G., Chou, C., Arendt, J. W., and Gindi, G. R., "Three-dimensional Radiographic Imaging with a Restricted View Angle," J. Opt. Soc. Am., 69 (1979) 1323-1333.
27. Frieden, B. R., "Restoring with Maximum Likelihood and Maximum Entropy," J. Opt. Soc. Amer., 62 (1972) 511-518.
28. Minerbo, G., "MENT: A Maximum Entropy Algorithm for Reconstructing a Source from Projection Data," Computer Graphics and Image Processing, 10 (1979) 48-68.
29. Tam, K. C., and Perez-Mendez, V., "Limits to Image Reconstruction from Restricted-Angular Input," to be presented at the IEEE 1980 Nuclear Science Symposium, Orlando, November 5-7, 1980; also to be published in IEEE Trans. Nucl. S., NS-28.
30. Papoulis, A., 1962, The Fourier Integral and Its Applications, (New York: McGraw-Hill) p. 44.

31. Whittaker, E. T., and Watson, G. N., 1952, A Course of Modern Analysis (England: Cambridge University Press) p. 67.

FIGURE CAPTIONS

Fig. 1. Two-dimensional imaging devices.

Fig. 2. Three-dimensional imaging devices.

Fig. 3. Point response function defined by an area element.

Fig. 4. A two-dimensional point response function $\phi_o(\underline{r})$ and its optical transfer function $\phi_o(\underline{k})$.

Fig. 5. A pyramidal three-dimensional point response function $\phi_o(\underline{r})$ and its optical transfer function $\phi_o(\underline{k})$.

Fig. 6. Space invariance of the point response function in the x dimension. If the edges of the detection cones generated at every point in the object do not intersect the vertical edges of the reconstruction region, the point response function is space invariant in the x dimension.

Fig. 7. Undeterminacy in the matrix method.

Fig. 8. Fourier transform iteration scheme for filling in missing-cone Fourier components.

Fig. 9. Radon transform iteration scheme for filling in missing projections.

Fig. 10. Schematic representations of the allowed cone and the object extent.

Fig. 11. Eigenvalues of BA for a 2-D problem for various half-angles of the allowed cone.

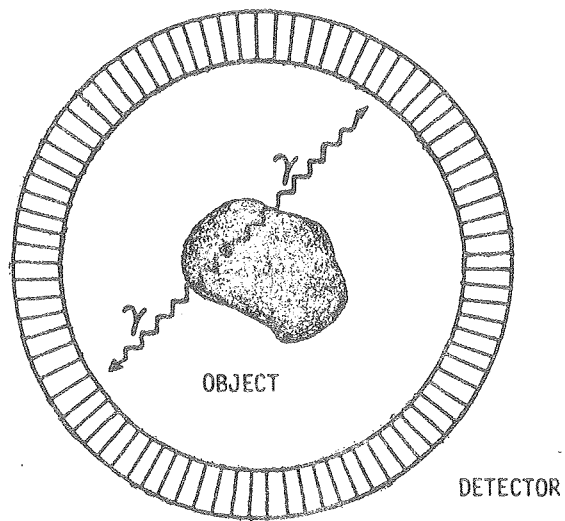
Fig. 12. Root mean square error of the reconstructed image of a 2-D phantom as a function of the number of iterations. The half-angle of the allowed cone is $\tan^{-1}(0.5)$.

Fig. 13. Root mean square error of the reconstructed image of a 2-D phantom after 20 iterations as a function of the half-angle of the allowed cone.

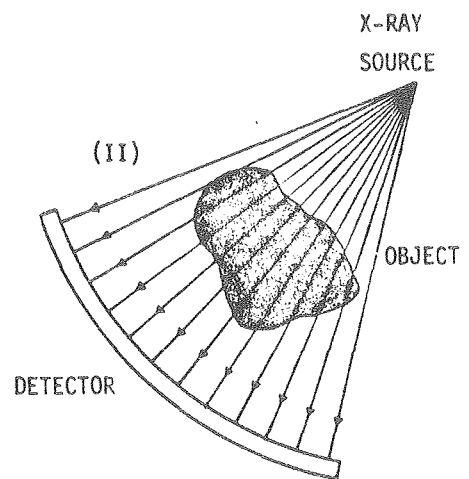
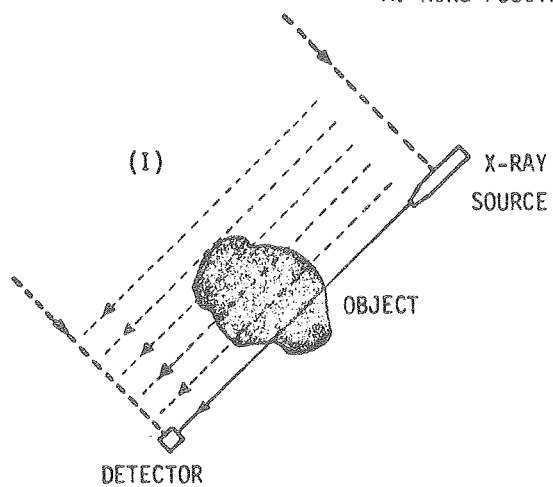
Fig. 14. Positive and negative density distributions of a point source whose missing-cone Fourier components have been set to zero. The half-angle of the allowed cone is $\tan^{-1}(0.5)$.

Fig. 15. A 11 x 11 square boundary representing the finite extent of an object within a 32 x 32 reconstruction area.

Fig. 16. Iteration scheme to stabilize the matrix method.

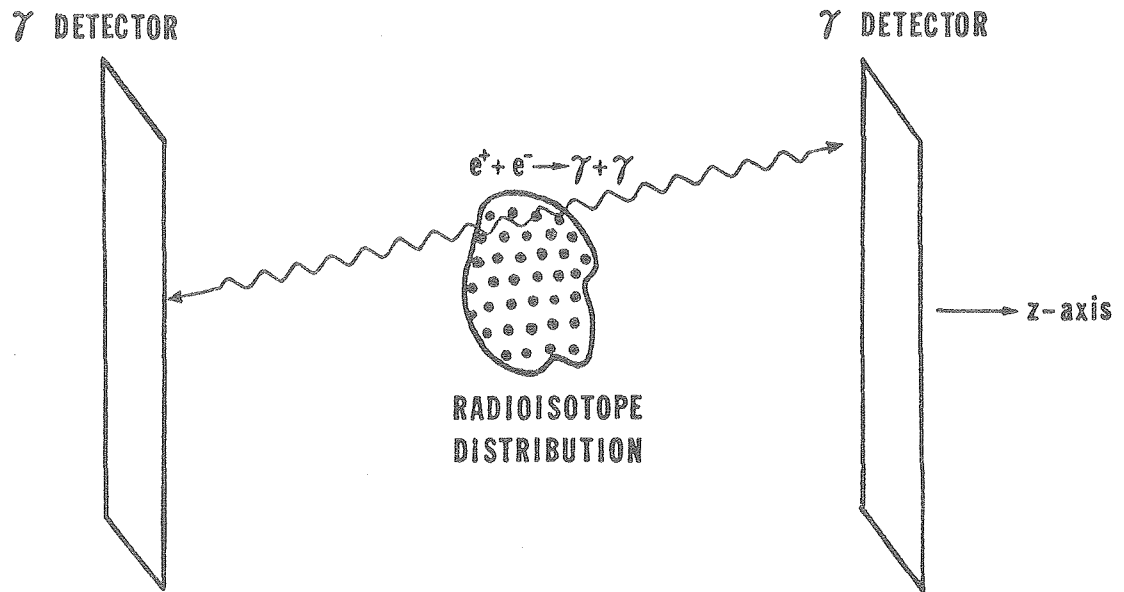


A. RING POSITRON CAMERA

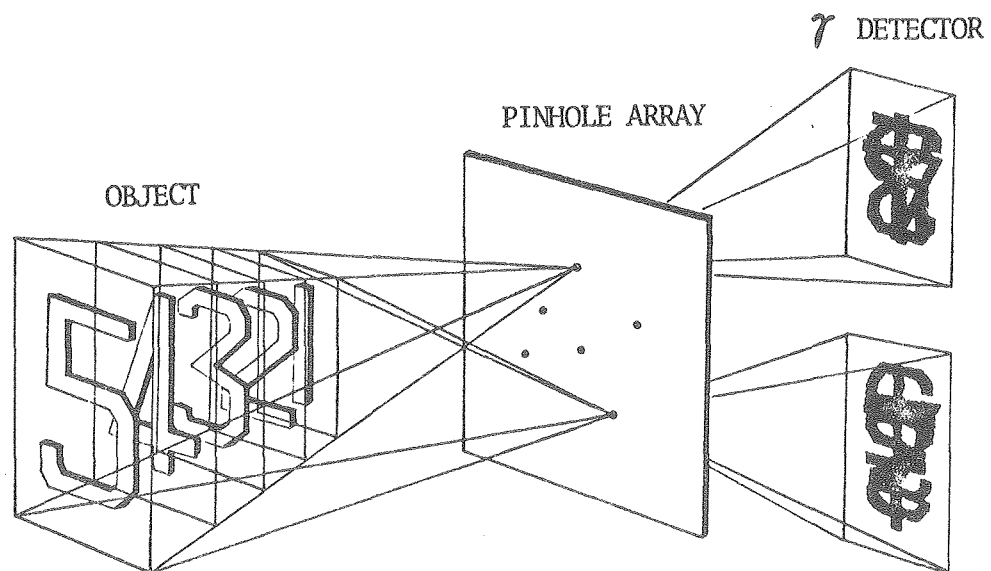


B. X-RAY SCANNING
(I) PARALLEL BEAM
(II) FAN BEAM

Figure 1



A. PLANAR POSITRON CAMERA



XBL 7812-13269

B. PINHOLE IMAGING DEVICE

Figure 2

$\phi_0(r)$

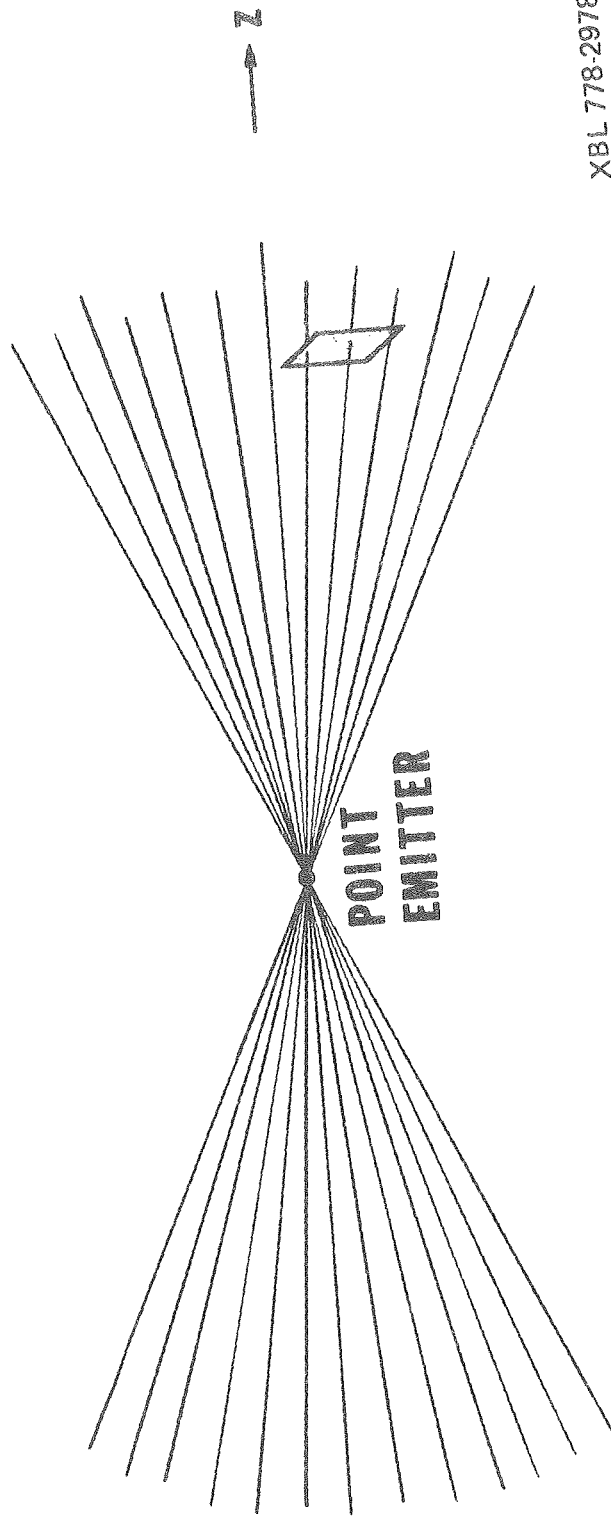
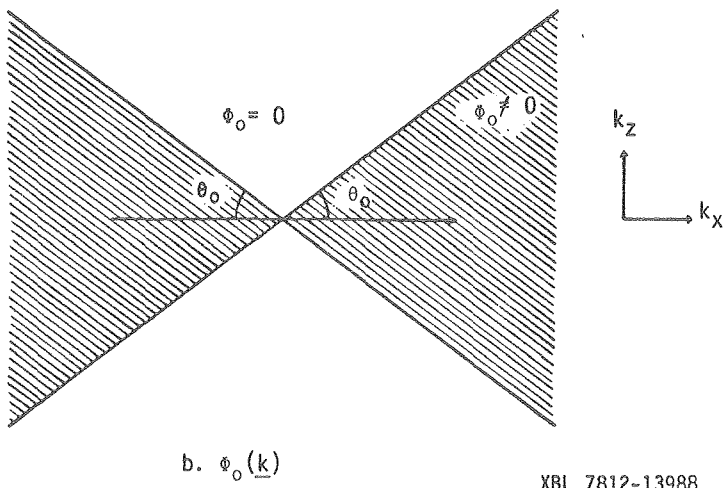
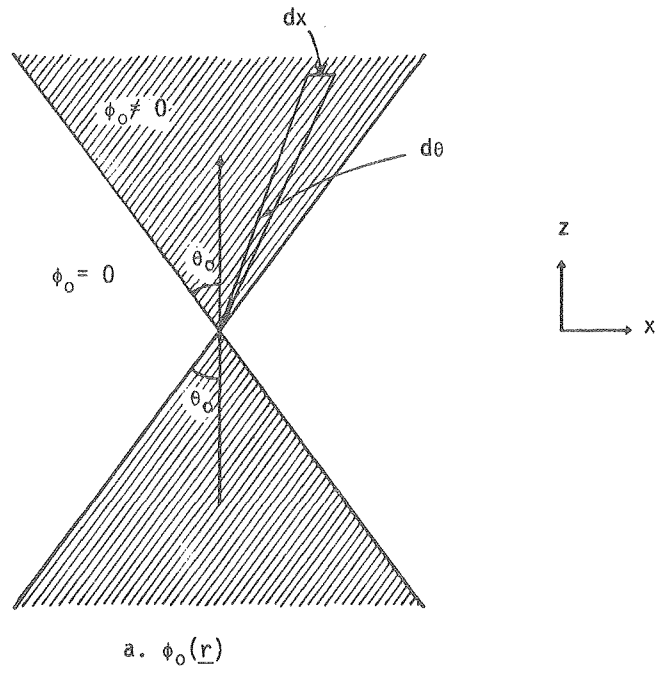
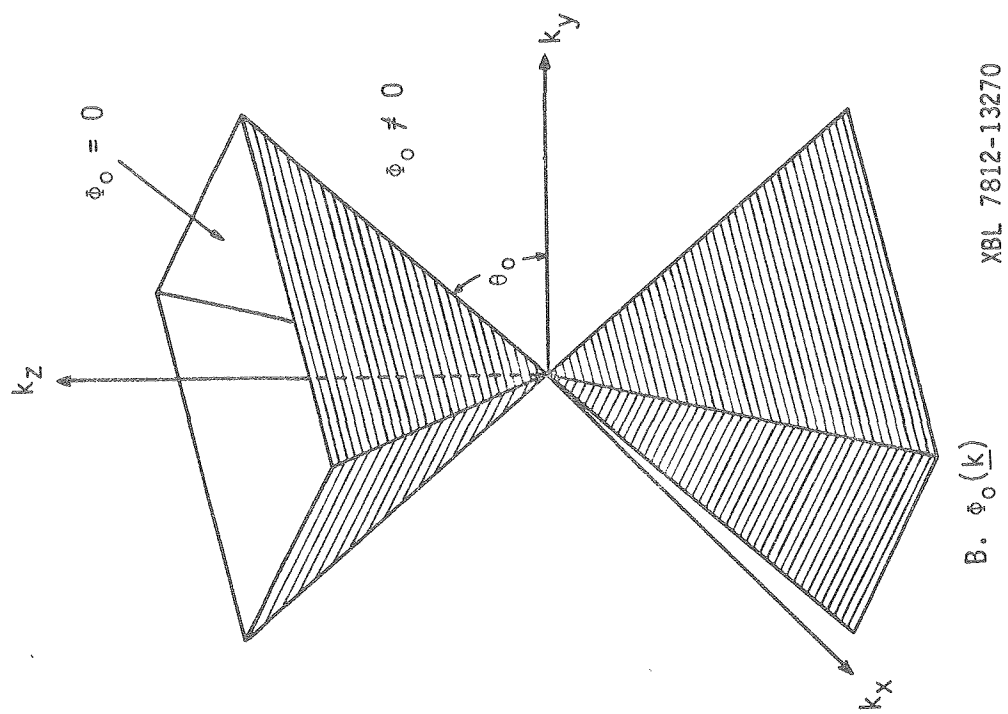
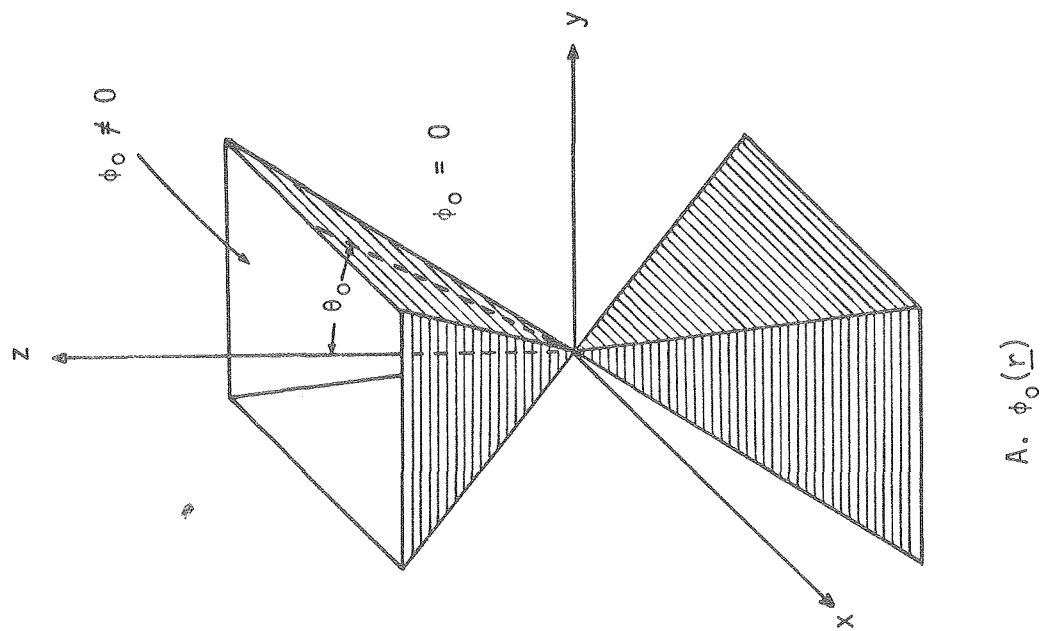


Figure 3



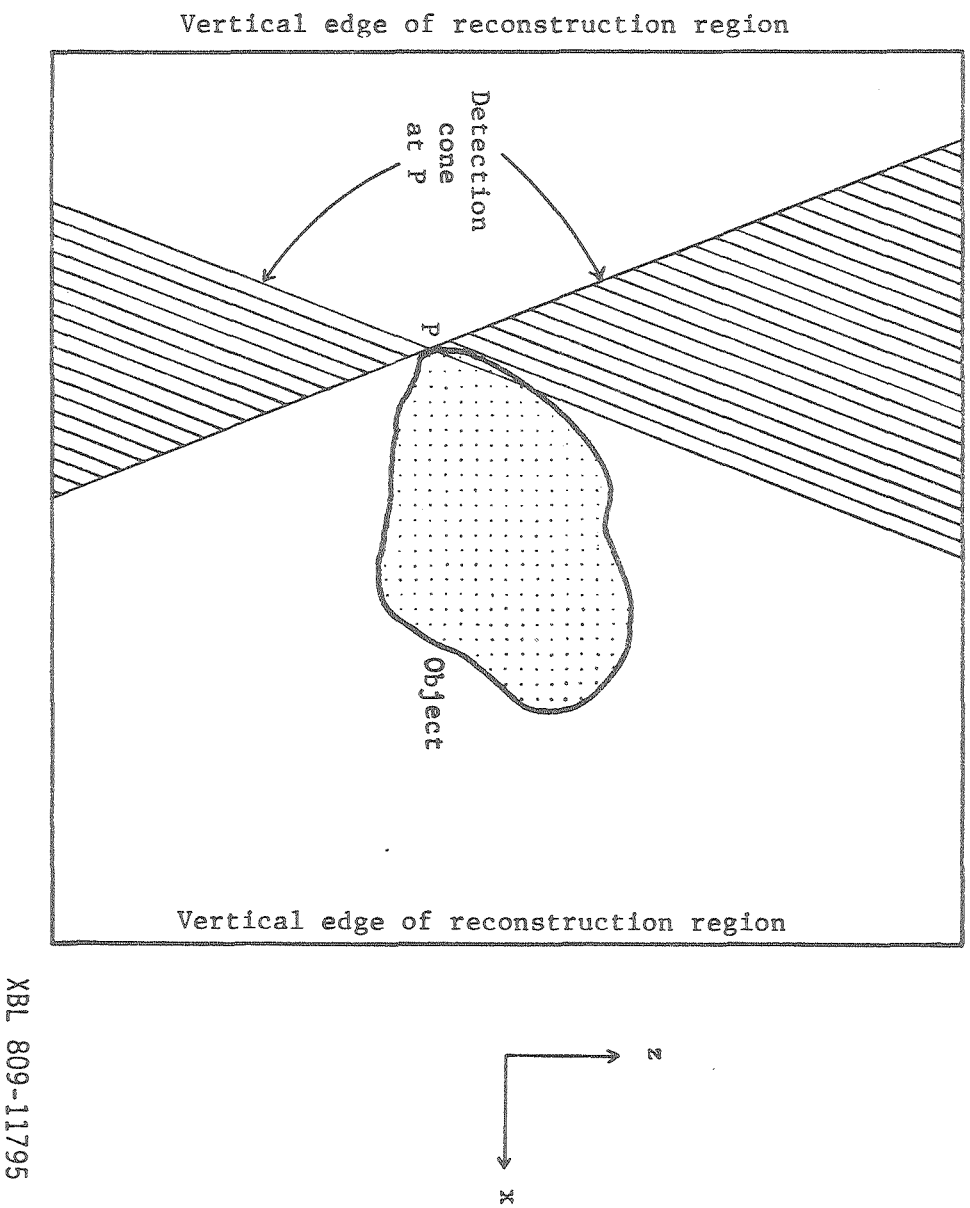
XBL 7812-13988

Figure 4



XBL 7812-13270

Figure 5



XBL 809-11795

Figure 6

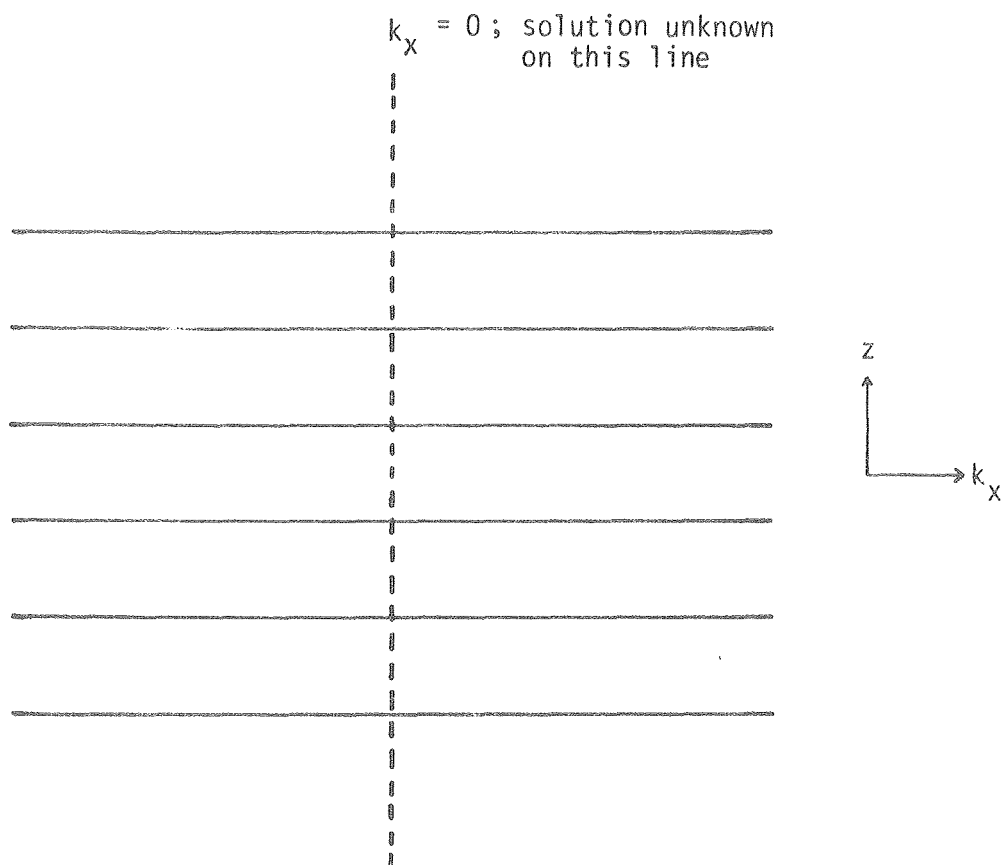


Figure 7

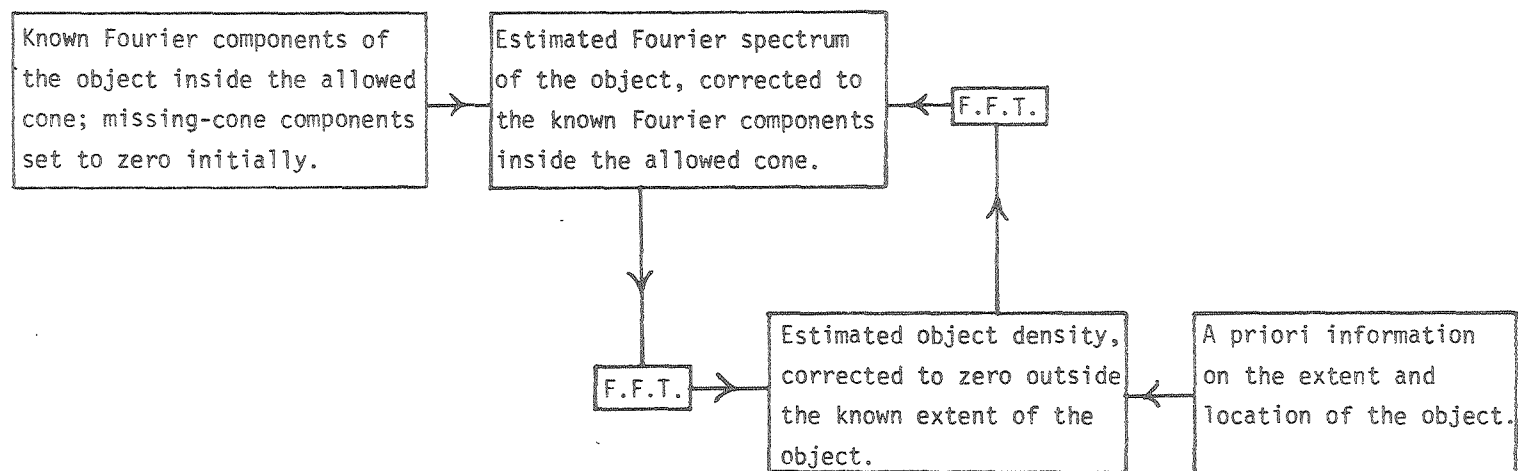


Figure 8

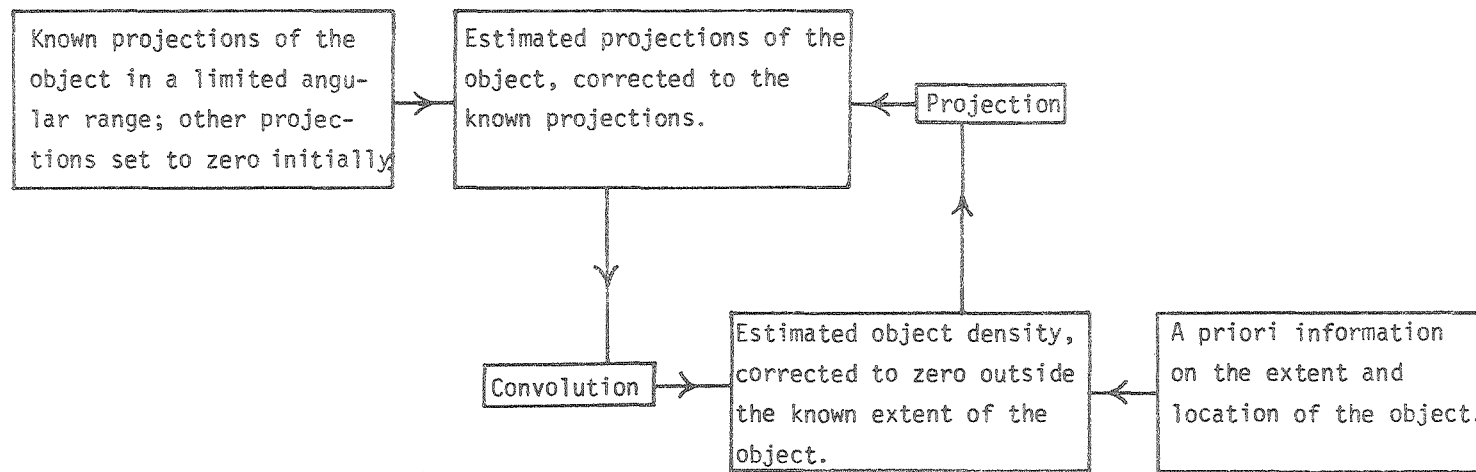
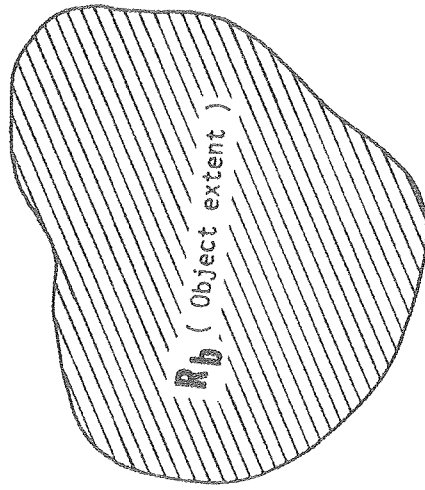
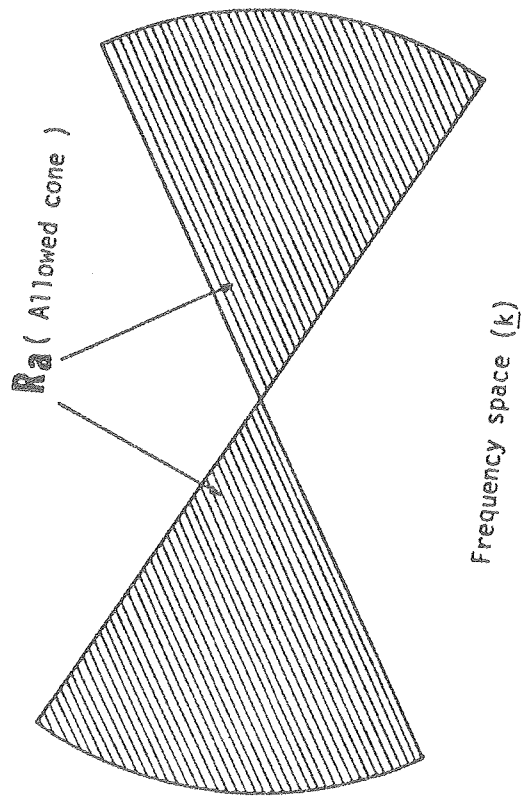


Figure 9



Object space (\bar{r})

XBL 809-11796

Figure 10

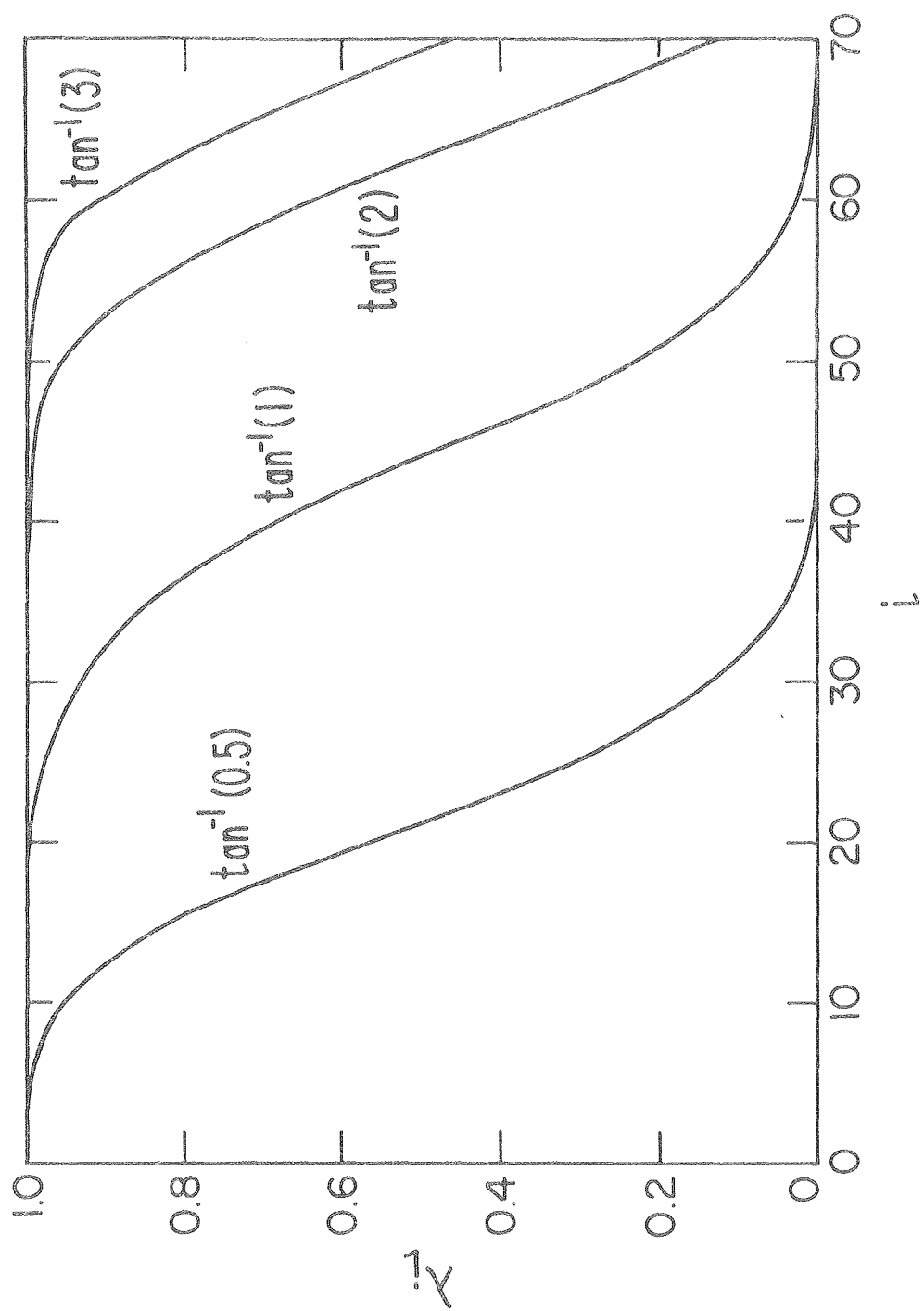


Figure 11

XBL 798-2379

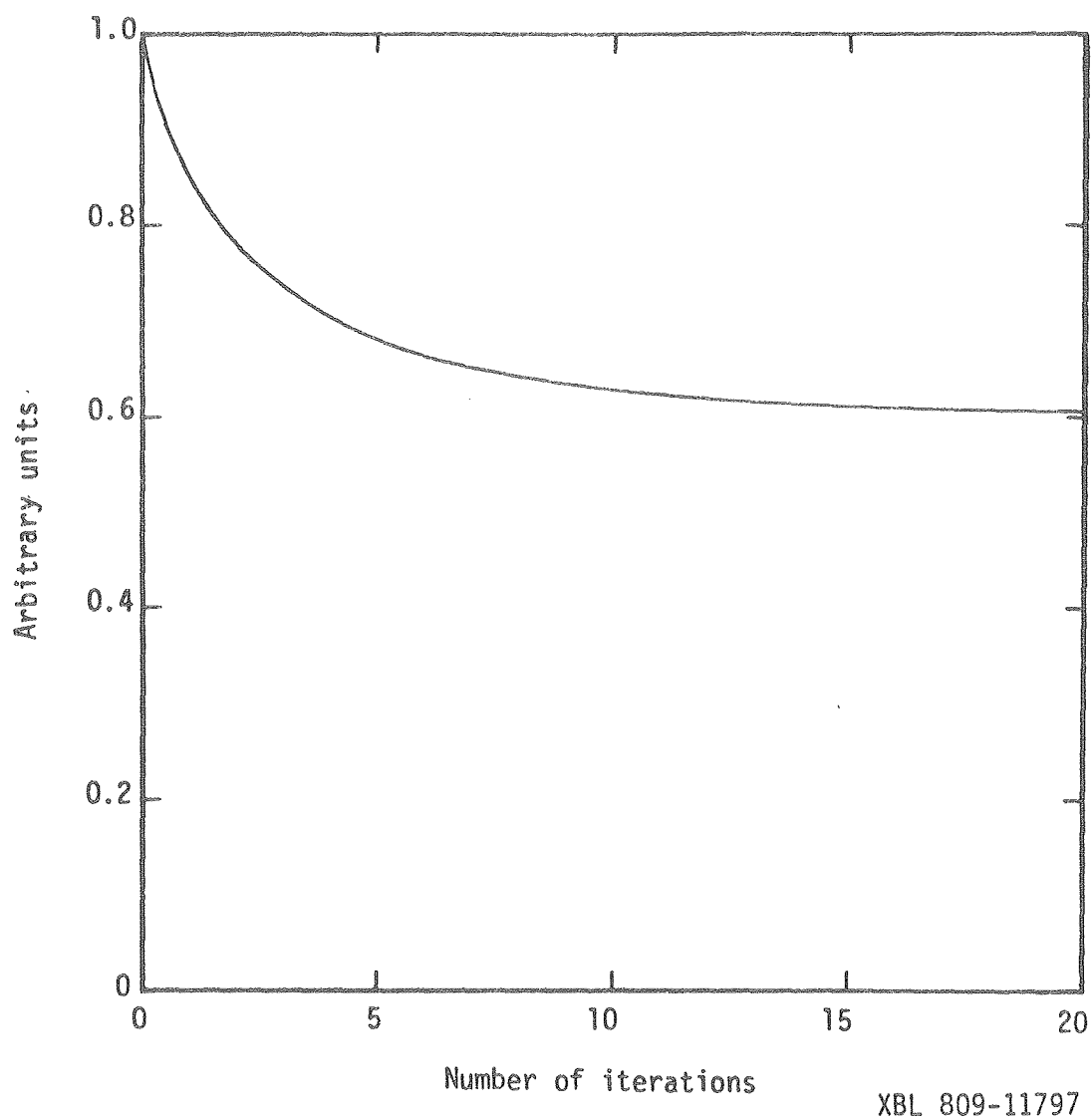
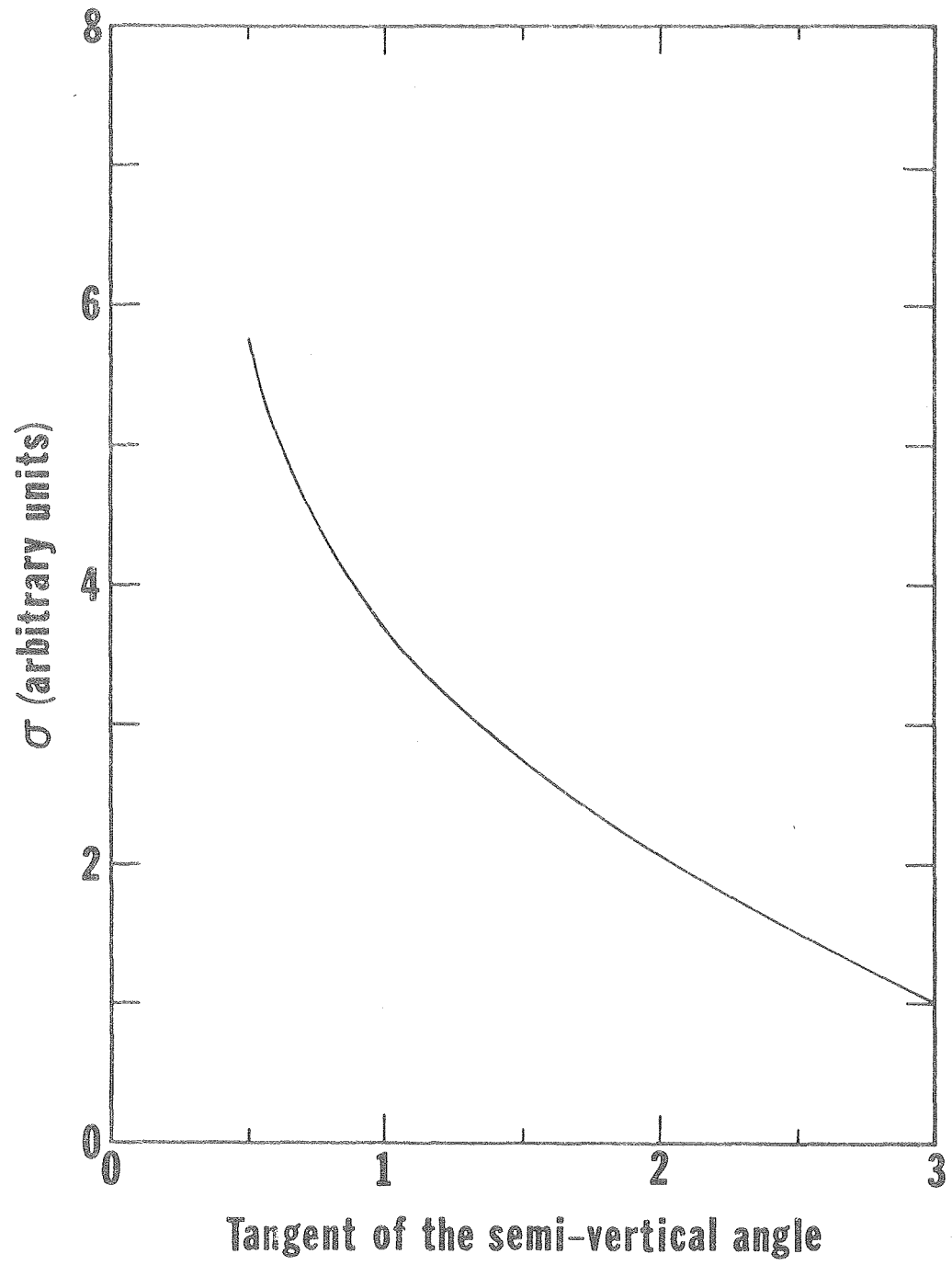
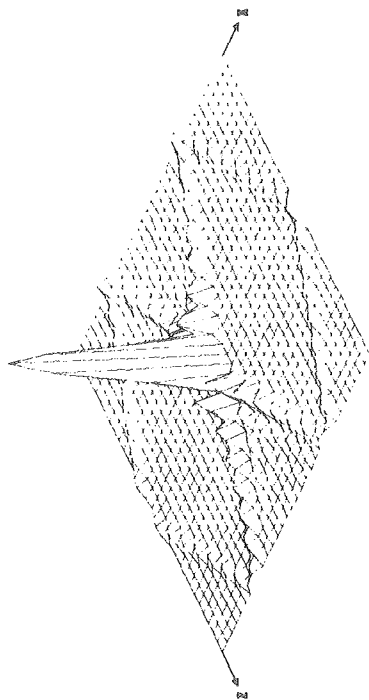


Figure 12

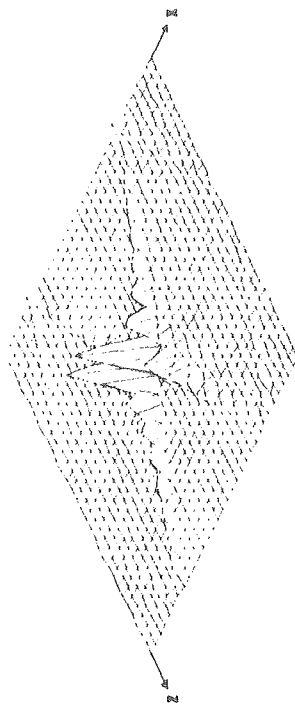


XBL 798-2378

Figure 13



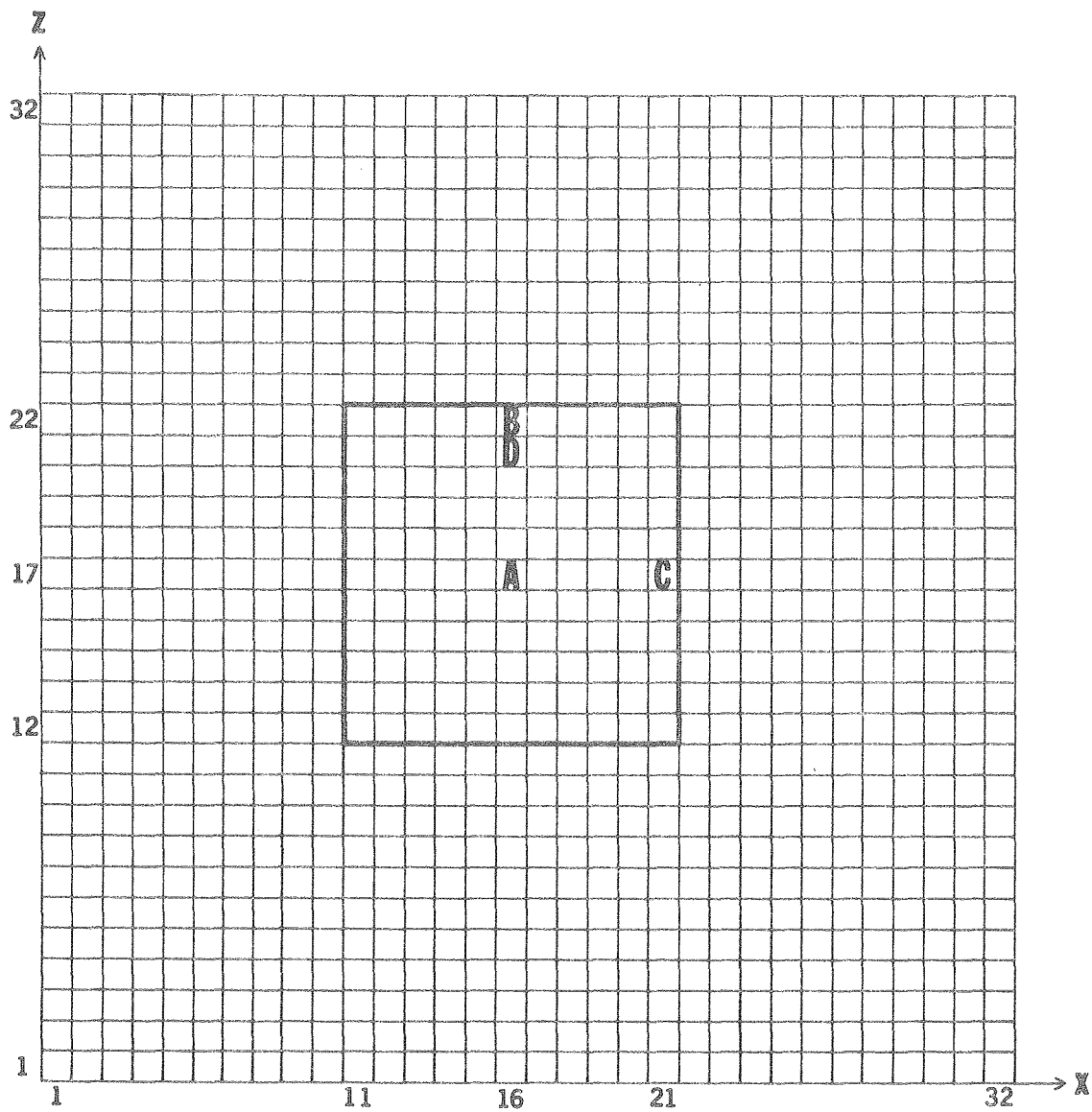
A. POSITIVE DENSITY DISTRIBUTION



B. NEGATIVE DENSITY DISTRIBUTION

XBL 802-8177

Figure 14



XBL 802-8176

Figure 15

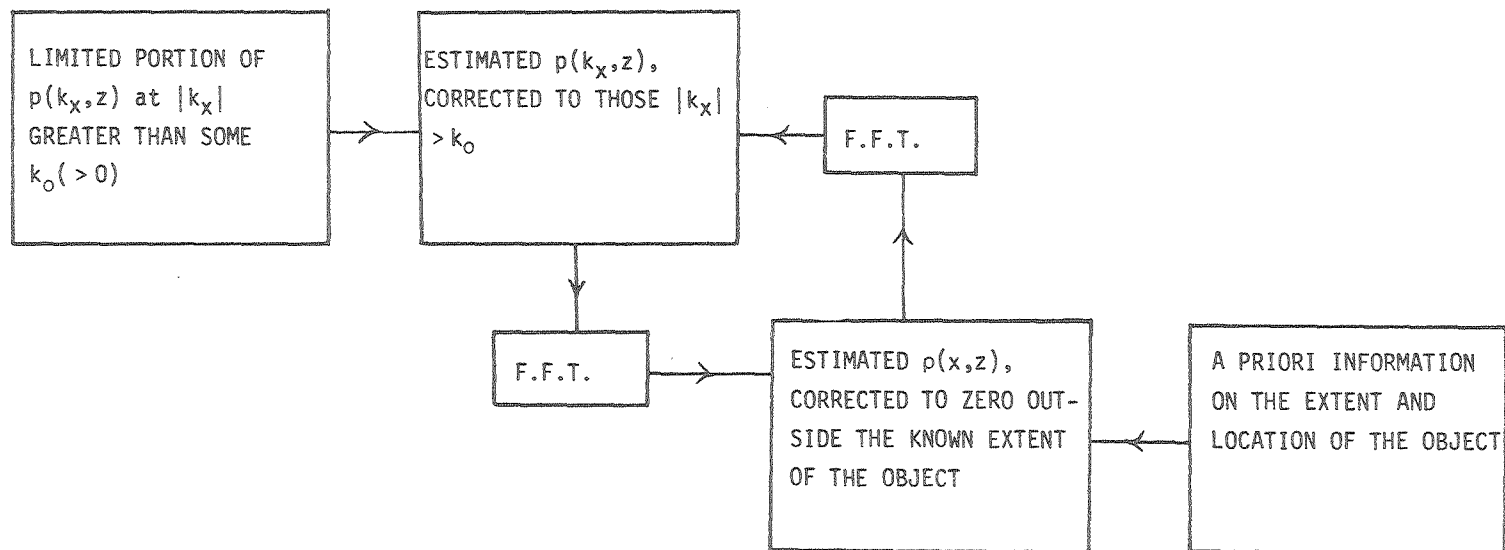


Figure 16